Draft version May 13, 2025
Typeset using LaTeX **preprint** style in AASTeX63

arXiv:2505.06476v1 [astro-ph.SR] 10 May 2025

Decimetric Type-IV Radio Bursts of Solar Flares Induced by Electron Cyclotron Maser Emission

Maoshui Lv[†] [1], Ze Zhong[†] [2,1], Xiangliang Kong[†] [1,2], Hao Ning [2,1], Feiyu Yu [1], Bing Wang [1], Baolin Tan [3], Victor Melnikov [4], Alexey Kuznetsov [5], Hongqiang Song [1], Ruisheng Zheng [1] and Yao Chen [2,1]

[1] *Institute of Space Sciences, Shandong University, Weihai, Shandong, 264209, China*
[2] *Center for Integrated Research on Space Science, Astronomy, and Physics, Institute of Frontier and Interdisciplinary Science, Shandong University, Qingdao 266237, China*
[3] *CAS Key Laboratory of Solar Activity, National Astronomical Observatories, Chinese Academy of Sciences, Beijing, 100012, China*
[4] *Central Astronomical Observatory at Pulkovo of the Russian Academy of Sciences, St Petersburg, 196140, Russia*
[5] *Institute of Solar-Terrestrial Physics, Irkutsk, 664033, Russia*

ABSTRACT

The radiation mechanism of decimetric wideband and pulsating radio bursts from the Sun (in terms of decimetric type-IV (t-IVdm) burst) and other flaring stars is a long-standing problem. Early investigations were based on the leading-spot hypothesis for the sun and yielded contradictory results. Here we provide essential evidence to support the scenario that these bursts are induced by the electron cyclotron maser emission (ECME) driven by energetic electrons mirrored in converging sunspot fields. This is done by analyzing 2 flare-associated t-IVdm bursts that are selected from a larger sample of 60 bursts recorded during 2010–2014, according to the levels of polarization and whether the source-field orientation can be unambiguously determined. We further modeled the transport of downward-streaming energetic electrons along a coronal loop and found most electrons get mirrored within the specific altitude range of 20–100 Mm. This explains why such bursts tend to have well-defined spectral ranges. The study greatly expands the application of ECME in solar radio astronomy and provides solar samples for similar bursts from other flaring stars.

Keywords: Solar radio emission (1522) — Solar flares (1496) — Solar activity (1475) — Solar magnetic fields (1503)

1. INTRODUCTION

Decimetric broadband radio bursts (with frequencies of hundreds of MHz to a few GHz) have been observed from the Sun (Young et al. 1961; De Groot 1970; Gotwols 1972) and other flaring stars (Güdel et al. 1989; Lang 1990; Bastian et al. 1990). In the solar case, such bursts have been classified as the decimetric type-IV bursts (t-IVdm). The bursts tend to have well-defined low and high-frequency cutoffs and are closely associated with flares. Their spectra often contain substantial fine structures, such as pulsations, spikes, zebras, fibers, and various absorption structures. This makes them distinct from their metric and centimetric counterparts.

Corresponding author: Yao Chen
yaochen@sdu.edu.cn
[†]These authors contributed equally to this work.

Due to the close proximity of the Sun to the Earth, solar radio astronomy has the advantage of high spectral and spatial observations. This favors the determination of the underlying radiation mechanism. Even so, the exact origin of solar t-IVdm bursts and their substantial fine structures remain largely unresolved (Bernold 1980; Benz 1980; Slottje 1982; Dulk 1985; Güdel & Benz 1988; Isliker & Benz 1994).

To determine the primary radiation mechanism, it is essential to identify the nature of the emission mode in terms of two freely escaping magnetoionic modes: extraordinary (X) or ordinary (O). This requires knowledge of the sense of polarization and orientation of the source magnetic field. Due to the lack of imaging data at decimetric wavelengths, to determine the source field orientation earlier studies (Aschwanden 1986; Zlobec et al. 1987) were based on the leading sunspot hypothesis that assumes the bursts originate from the leading spots of the associated flares. Contradictory conclusions

were drawn by these studies. As a result, distinct mechanisms have been proposed: plasma emission (PE; Kuijpers 1974, 1980; Zaitsev & Stepanov 1975; Benz & Kuijpers 1976), electron cyclotron maser emission (ECME; Benz & Tarnstrom 1976; Aschwanden & Benz 1988a,b), or gyrosynchrotron radiation.

Over the past eight decades of solar radio astronomy, only one type of solar radio bursts — spikes — is convincingly attributed to ECME, while several other types of solar bursts such as type-I, II, and III have been attributed to PE. Recent studies have reported a rare ECME-like event with week-long decimetric pulsations. The event is not directly associated with any specific flare (Yu et al. 2024; Sharma et al. 2024). Here we investigated flare-induced t-IVdm bursts using extreme ultraviolet (EUV) and radio imaging observations. Among the 60 t-IVdm events recorded during 2010–2014, we found 2 flare-associated bursts with medium-strong levels of polarization and from sources near a sunspot where the field orientation can be determined. For both bursts, the maximum brightness temperature (T_B) exceeds 10^{10} K and their sources coincide with the sites of the second harmonic of the extrapolated local electron gyrofrequency. These findings provide substantial evidence that the flare-induced t-IVdm bursts are mainly the harmonic X-mode radiated via ECME. By modeling the electron transport along a given loop, we further suggest these bursts are excited by energetic electrons mirrored in converging sunspot fields and elaborate why such t-IVdm bursts tend to have well-defined spectral cutoffs. In Section 2, we introduce the data and event selection, followed by modeling methods in Section 3. The results are presented in Section 4 and the discussion is provided in Section 5.

2. OBSERVATIONS AND DATA ANALYSIS

2.1. *Data and Instruments*

The t-IVdm bursts were identified using the Bleien 7m radio telescope, which covers 175 to 870 MHz with a temporal resolution of 0.25 seconds. The Nançay Radioheliograph (NRH; Kerdraon & Delouis 1997) offers imaging data with polarization measurements at 10 frequencies spanning from 150 to 445 MHz. The spatial resolution depends on the frequency and time of observation, being $\sim 2'$ at 445 MHz and $\sim 6'$ at 150 MHz in the summer, and up to three times larger along the north-south direction in the winter.

The Solar Dynamics Observatory (SDO; Pesnell et al. 2012) provides EUV data with the Atmospheric Imaging Assembly (AIA; Lemen et al. 2012) and magnetograms with the Helioseismic and Magnetic Imager (HMI; Scherrer et al. 2012). The EUV data have a pixel size of $0.6''$ and a cadence of 12 s.

2.2. *Event Selection*

We collected t-IVdm bursts based on the data from the Bleien observatory in the frequency range of 175–870 MHz. To tell the location of the radio sources and the magnetic field orientation therein, we retained events observed during 2010–2014 when both radio and EUV imaging data were available and the radio data recorded by NRH were calibrated in both polarization and T_B.

According to the general definition of t-IVdm bursts, we selected events with the maximum frequency exceeding 300 MHz, the bandwidth wider than 100 MHz, and the duration longer than 5 minutes. This yielded 60 events, from which we selected 37 flare-associated events (Table 1) according to the following criteria: the burst should be within 30 minutes around the peak of a flare, which originates from the active region associated with the NRH sources.

To identify the radiation mode, we only retained events with a high to moderate level of polarization (>30%) whose sources are located near a sunspot, with both latitude and longitude within 60°, to ensure an unambiguous determination of the source-field orientation. The field orientation is further verified by the nonlinear force-free field (NLFFF) extrapolation. After applying these criteria, we identified 2 events.

3. MODELING METHODS

3.1. *Magnetic Field Processing and Extrapolation*

We analyzed the HMI vector magnetic field data ("hmi.B_720s"), which cover the full solar disk with a temporal cadence of 720 s and a spatial resolution of $0.505''$ (Schou et al. 2012). The coronal magnetic field was reconstructed using the magneto-frictional method (Guo et al. 2016). To do this, we first corrected the projection effect (Gary & Hagyard 1990) since the active region is away from the disk center, and then removed the residual force on the magnetograms using a preprocessing method (Wiegelmann et al. 2006). We applied two metrics (Wheatland et al. 2000) to check whether the magnetic field reaches the force-free state or not. The obtained force-freeness metrics for both events are lower than 0.25, and the divergence-freeness metrics are close to 8×10^{-5} , similar to previous studies (Zhong et al. 2019).

3.2. *Particle Transport Modeling*

Following our previous studies (Kong et al. 2022, 2025), we modeled the transport of energetic electrons in the coronal loop by solving the focused transport equation numerically (Roelof 1969; Skilling 1971; Effenberger

& Petrosian 2018). Here, we only considered the magnetic mirroring effect and neglected the pitch-angle scattering by turbulence or Coulomb collision. The reduced particle transport equation is written as:

$$\frac{\partial f}{\partial t} = -v\mu\hat{\mathbf{b}}\cdot\nabla f - \frac{v(1-\mu^2)}{2L_B}\frac{\partial f}{\partial \mu} \quad (1)$$

where f is the particle distribution function, v is the particle speed, μ is the pitch-angle cosine, and t is the time. The terms on the right-hand side describe the energetic electrons streaming along the direction of the magnetic field $\hat{\mathbf{b}}$ and the magnetic mirroring effect with the focusing length $L_B = \left(\hat{\mathbf{b}}\cdot\nabla \ln B\right)^{-1}$.

Since the above equation is basically a Fokker-Planck equation, it is mathematically equivalent to a set of stochastic differential equations (SDEs; Zhang 1999; Strauss & Effenberger 2017). Here, we employed the time-forward SDEs to trace the particle's position and pitch-angle (Kong et al. 2022, 2025).

In the simulations, we assumed that the accelerated electrons have a Gaussian distribution in pitch-angle, $f(\mu) \sim \exp\left(-\frac{(\mu-1)^2}{0.01}\right)$ with a power-law energy spectrum of $f(E) \sim E^{-3}$ with E ranging from 10 to 100 keV. The electrons are impulsively released in the upper section of the selected loop, given by $x = [-484, -454]$ Mm, $y = [31, 51]$ Mm, and $z = [150, 170]$ Mm. We injected a total of 10 million pseudo-particles for the simulation. We obtained the 3D spatial distribution, pitch-angle and velocity-space distribution of energetic electrons at different times.

4. RESULTS

4.1. *Multiwavelength data analysis for the 20110924 event*

Fig. 1 presents the spectra of the t-IVdm burst, along with the NRH data for T_B and polarization. The event occurred from 12:50 to 13:50 UT and consists of two major sub-bursts (Bursts I and II), each lasting ∼20 minutes. The observations reveal three features: (1) Both burst components are highly intermittent, with well-defined upper and lower frequency cutoffs at ∼1–2 GHz and 200–300 MHz, respectively. (2) The maximum T_B is $\sim 2\times10^{11}$ K for Burst I and $\sim 4\times10^{10}$ K for Burst II. (3) The polarization is left-handed with levels reaching ∼70–100%, with an overall increasing trend with frequency. Based on these observations, we conclude that the emission is coherent since the incoherent gyrosynchrotron radiation of solar flares cannot yield such intermittency with high T_B and strong polarization at such frequencies (Dulk 1985; Gary & Keller 2004).

Fig. 2 and the animation 1 present the eruption recorded by AIA at 94, 131, and 171 Å, superposed by the NRH source contours at 8 frequencies from 228 to 445 MHz. This event was associated with an M7.1-class flare originating from NOAA Active Region (AR) 11302. The flare started at 12:33 UT, peaked at 13:17 UT, and ended at 14:10 UT. The AR has a complex multipolar topology with three sunspots. The event was associated with a halo coronal mass ejection. Both 94 and 131 Å data show the eruption of a hot structure and the rise of heated post-flare loops (Fu et al. 2023).

The NRH sources moved systematically during the burst, exhibiting at least two leaps since 12:50 UT. These leaps indicated the start of bursts I and II. Around 13:00 UT, the sources moved to the region above the flaring loops, and at ∼13:20 UT, they leaped toward the western leg of the loops, right above the rightmost sunspot with a negative polarity. During the whole process, the NRH sources aligned well with each other, and higher-frequency sources are closer to the disk.

Using the NLFFF extrapolation method, we deduced the coronal field lines of the AR (Figs. 2d and 2h), and overlaid them onto the HMI magnetogram. The field lines are color-coded to represent the section where the field strength varies from ∼40.7 G (blue) to ∼79.5 G (red), which correspond to the local second harmonic gyrofrequency ($2\ \Omega_{ce}$) increasing from 228 to 445 MHz.

We draw two major conclusions: (1) NRH sources of both bursts (I and II) lie along the field lines pointing toward the sunspot with strong left-handed polarization (Fig. 1c), so both bursts are of X mode, and (2) the sources align well with the colored $2\ \Omega_{ce}$ section. Thus, the most likely radiation mechanism is the harmonic X mode via ECME since the alternative coherent plasma emission process would produce O mode for the fundamental branch or weak polarization for the harmonic branch (Dulk 1985; Melrose et al. 1978; Melrose 2017; Ni et al. 2020; Chen et al. 2022; Zhang et al. 2022).

4.2. *Modeling particle transport for the 20110924 event*

Magnetic field lines converge toward the sunspot as their strength increases, forming a magnetic mirror within which energetic electrons can be reflected. Around the mirroring point, the electron pitch angle (θ) is ∼90° and the kinetic energy is mainly carried by the perpendicular motion. At locations with sufficient mirrored electrons, the electron velocity distribution function (VDF) shall develop significant positive gradient (i.e., $\partial f/\partial v_\perp > 0$), which can excite ECME to radiate preferentially in X mode (Twiss 1958; Wu & Lee 1979; Ning et al. 2021; Yousefzadeh et al. 2021).

To demonstrate whether the above scenario applies, we selected an extrapolated field line (the cyan line in Fig. 2h) that clusters the NRH sources. The field

strength B increases rapidly with decreasing altitude (the blue line in Fig. 3a), from ∼4.0 G at 160 Mm, to ∼14.5 G at 100 Mm, and reaching ∼351.8 G at 20 Mm. The critical pitch angles are given by $\theta_c = \arcsin\sqrt{B_0/B_m}$ (the red line in Fig. 3a), where B_0 and B_m are field strengths at the release and mirroring points, respectively. According to the basic theory of magnetic mirror, θ_c are 31.7° at 100 Mm and 6.1° at 20 Mm. This large change of θ_c implies a significant population of downward-propagating energetic electrons will get reflected within this range of altitude, as simulated below.

To simulate the transport of energetic electrons that stream down toward the sunspot after being accelerated high in the corona, we release a population of Gaussian-distributed beam-like energetic electrons in the upper loop section (see the yellow sphere in Fig. 2h at an altitude of 160 Mm). The electrons, with the distribution of $f(\mu) \sim \exp\left(-\frac{(\mu-1)^2}{0.01}\right)$ where $\mu = \cos\theta$, first stream toward the negative sunspot and then get mirrored at different altitudes (Fig. 3b and the animation 2). As shown in Fig. 3c, a large fraction of 20–30 keV electrons get mirrored at heights above ∼10–20 Mm within 2 seconds after release, among them ∼85% (97%) have pitch angles exceeding 90° (60°). Eventually, ∼89.7% of all injected electrons are mirrored at heights between 20 and 100 Mm (Fig. 3d). This result also holds for 10–20 keV, 30–50 keV, and 50–100 keV electrons since the mirroring point only depends on the initial pitch angles of particles.

As expected, the electrons within 20–100 Mm exhibit a shell-like VDF (Fig. 4), with significant positive gradient in the perpendicular direction. This drives the ECME to release both the fundamental X mode (X1) and the harmonic X mode (X2). According to the latest particle-in-cell simulation (Yousefzadeh et al. 2021) with similar numerical setup, energetic electrons with such shell-like VDFs excite the X2 mode more efficiently than the X1 mode. In addition, X1 experiences strong absorption at the corresponding second harmonic layer and thus cannot escape freely (Melrose & Dulk 1982; Robinson 1989; McKean et al. 1989; Melrose & Wheatland 2016). Therefore, the X2 mode is relevant to the t-IVdm bursts observed from the Earth. Note that the ECME-radiating energetic electrons within such converging field are characterized by the shell or strip-like VDFs, rather than the generally-presumed loss-cone distribution.

Based on the above analysis, the spectral cutoffs of t-IVdm bursts are due to the limited ranges of altitudes (∼20–100 Mm) within which most energetic electrons get mirrored. This altitude range corresponds to ECME-induced harmonic frequencies (∼2 Ω_{ce}) of ∼80 to 2000 MHz. This explains the generally well-defined spectral ranges of most t-IVdm bursts.

4.3. *The 20120614 event*

We further investigated the t-IVdm event on 14 June 2012 (see Appendix). The burst displays intermittent characteristics with a maximum T_B of ∼2×10^{10} K and exhibits strong levels of left-handed polarization (50–100%). During most time of the burst, the NRH sources are above a negative spot and coincide spatially with the corresponding extrapolated 2 Ω_{ce} section. This further supports the burst is excited via ECME at the X2 mode.

5. DISCUSSION

This study highlights the critical role of ECME in generating the commonly-observed wideband pulsating decimetric radio bursts. This has profound implication, not only to solar astronomy but also to stellar physics, since the ECME radiation helps in diagnosing the source field strength that remains a major challenge even in the solar case.

For the other 58 events collected here, we cannot determine the magnetic field orientation within the sources or the sources are characterized by weak polarizations. So their radiation mechanisms remain elusive. For events occurring after 2014, we cannot determine the sense of polarization because NRH stopped calibrating its polarization data since then. Further development of decimetric radio heliograph with well-calibrated data of high spatial and spectral resolution is demanded for a better understanding of such events.

ACKNOWLEDGMENTS

The authors are grateful to the GOES, NRH, SDO/AIA, and HMI consortia for providing the data. We thank the Institute for Data Science FHNW Brugg/Windisch, Switzerland, for providing the e-Callisto data. SDO is a mission of NASA's Living With a Star Program. This work was supported by the National Natural Science Foundation of China (12303061, 12127901, 12333009, 42074203 and 12203031), the National Key R&D Program of China under grant (2022YFF0503002 and 2022YFF0503000), the Shandong Natural Science Foundation of China (ZR2023QA074), and the China Postdoctoral Science Foundation (2023T160385, 2022M711931, and 2022TQ0189). A.K. was supported by the Ministry of Science and Higher Education of the Russian Federation. We acknowledge the computational resources provided by the Beijing Super Cloud Computing Center (BSCC, URL: http://www.blsc.cn).

APPENDIX

The t-IVdm event on June 14 2012

Fig. S1 presents the spectra of the event, along with the NRH data of T_B and polarization levels. The spectra span from ∼150 MHz to above 5 GHz, and can be divided into two components: the gyrosynchrotron emission at higher frequencies (∼500 MHz – >5 GHz) peaking around 2 GHz, and the t-IVdm emission below ∼500 MHz. The t-IVdm burst starts from 13:40 to 15:20 UT, with T_B decreasing with increasing frequency, being distinct from the usual optically thick gyrosynchrotron emission.

According to Fig. S1, the t-IVdm burst exhibits the following characteristics: (1) It is intermittent with a well-defined lower frequency cutoff of ∼150–200 MHz, and the upper frequency cutoff is ∼500 MHz when it can be clearly separated from the gyrosynchrotron component. (2) The maximum T_B is $\sim 2 \times 10^{10}$ K. (3) At most NRH frequencies, the burst manifests strong left-handed polarization with a level of ∼50–100%. At 445 MHz from 14:14 to 14:16 UT, it presents a right-handed polarization with a level of ∼30%.

Fig. S2, along with the animation 3, display the eruption observed by AIA at 94, 131, and 171 Å, superposed by the NRH source contours at 9 frequencies from 150 to 445 MHz. The event was associated with two M-class flares (M1.5 and M1.9) and a halo coronal mass ejection originating from NOAA AR 11504 that has two large spots with opposite polarities. The M1.5-class flare began at 12:47 UT, peaked at 14:08 UT, and ended at 15:00 UT while the M1.9-class flare started at 12:52 UT, reached its peak at 14:35 UT, and ended at 15:56 UT. Both 94 and 131 Å data reveal the eruption of hot structures, followed by heated post-flare loops.

Similar to the event on 24 September 2011, the NRH sources align well with higher-frequency sources being closer to the disk. During the burst, the sources move systematically with at least two leaps. Before 13:50 UT, the sources lie above the east footpoint of the flaring loops, right above the left negative sunspot. Subsequently, the sources move to the region above the flaring loops. From ∼14:10 to ∼14:17 UT, they are located near the west footpoint of the loops, above the right positive sunspot. At ∼14:20 UT, the sources return to the region above the left spot.

Figs. S2d and S2h present the extrapolated field lines and NRH sources, overplotted onto the HMI magnetogram. The field lines are color-coded to depict the section where the field strength varies from ∼26.8 G (blue) to ∼79.5 G (red). The corresponding second harmonic gyrofrequency (2 Ω_{ce}) increases from 150 to 445 MHz. The NRH sources align well with the field lines pointing toward the sunspot and being co-spatial with the colored 2 Ω_{ce} section.

As mentioned, the sources at 445 MHz show moderate level of right-handed polarization from 14:14 to 14:16 UT. This occurs when the sources are close to the positive spot, indicating the radiation is also in X mode.

We summarize that the 20120614 burst is also in the X2 mode radiated coherently via ECME.

REFERENCES

Aschwanden, M. J. 1986, SoPh, 104, 57, doi: 10.1007/BF00159947

Aschwanden, M. J., & Benz, A. O. 1988a, ApJ, 332, 447, doi: 10.1086/166669

—. 1988b, ApJ, 332, 466, doi: 10.1086/166670

Bastian, T. S., Bookbinder, J., Dulk, G. A., & Davis, M. 1990, ApJ, 353, 265, doi: 10.1086/168613

Benz, A. O. 1980, ApJ, 240, 892, doi: 10.1086/158303

Benz, A. O., & Kuijpers, J. 1976, SoPh, 46, 275, doi: 10.1007/BF00149857

Benz, A. O., & Tarnstrom, G. L. 1976, ApJ, 204, 597, doi: 10.1086/154208

Bernold, T. 1980, A&AS, 42, 43

Chen, Y., Zhang, Z., Ni, S., et al. 2022, ApJL, 924, L34, doi: 10.3847/2041-8213/ac47fa

De Groot, T. 1970, SoPh, 14, 176, doi: 10.1007/BF00240176

Dulk, G. A. 1985, ARA&A, 23, 169, doi: 10.1146/annurev.aa.23.090185.001125

Effenberger, F., & Petrosian, V. 2018, ApJL, 868, L28, doi: 10.3847/2041-8213/aaedb3

Fu, W., Guo, Y., Ding, M., Zhong, Z., & Qiu, Y. 2023, ApJ, 944, 179, doi: 10.3847/1538-4357/acb6fb

Gary, D. E., & Keller, C. U., eds. 2004, Astrophysics and Space Science Library, Vol. 314, Solar and Space Weather Radiophysics - Current Status and Future Developments

Gary, G. A., & Hagyard, M. J. 1990, SoPh, 126, 21, doi: 10.1007/BF00158295

Gotwols, B. L. 1972, SoPh, 25, 232, doi: 10.1007/BF00155759

Güdel, M., & Benz, A. O. 1988, A&AS, 75, 243

Güdel, M., Benz, A. O., Bastian, T. S., et al. 1989, A&A, 220, L5

Guo, Y., Xia, C., Keppens, R., & Valori, G. 2016, ApJ, 828, 82, doi: 10.3847/0004-637X/828/2/82

Isliker, H., & Benz, A. O. 1994, A&AS, 104, 145

Kerdraon, A., & Delouis, J.-M. 1997, in Coronal Physics from Radio and Space Observations, ed. G. Trottet, Vol. 483, 192, doi: 10.1007/BFb0106458

Kong, X., Ning, H., & Chen, Y. 2025, Frontiers in Astronomy and Space Sciences, 11, 1510579, doi: 10.3389/fspas.2024.1510579

Kong, X., Chen, B., Guo, F., et al. 2022, ApJL, 941, L22, doi: 10.3847/2041-8213/aca65c

Kuijpers, J. 1974, SoPh, 36, 157, doi: 10.1007/BF00151557

Kuijpers, J. 1980, in IAU Symposium, Vol. 86, Radio Physics of the Sun, ed. M. R. Kundu & T. E. Gergely, 341–360, doi: 10.1017/S0074180900037098

Lang, K. R. 1990. https://api.semanticscholar.org/CorpusID:119679538

Lemen, J. R., Title, A. M., Akin, D. J., et al. 2012, SoPh, 275, 17, doi: 10.1007/s11207-011-9776-8

McKean, M. E., Winglee, R. M., & Dulk, G. A. 1989, SoPh, 122, 53, doi: 10.1007/BF00162828

Melrose, D. B. 2017, Reviews of Modern Plasma Physics, 1, 5, doi: 10.1007/s41614-017-0007-0

Melrose, D. B., & Dulk, G. A. 1982, ApJ, 259, 844, doi: 10.1086/160219

Melrose, D. B., Dulk, G. A., & Smerd, S. F. 1978, A&A, 66, 315

Melrose, D. B., & Wheatland, M. S. 2016, SoPh, 291, 3637, doi: 10.1007/s11207-016-1006-y

Ni, S., Chen, Y., Li, C., et al. 2020, ApJL, 891, L25, doi: 10.3847/2041-8213/ab7750

Ning, H., Chen, Y., Ni, S., et al. 2021, A&A, 651, A118, doi: 10.1051/0004-6361/202140427

Pesnell, W. D., Thompson, B. J., & Chamberlin, P. C. 2012, SoPh, 275, 3, doi: 10.1007/s11207-011-9841-3

Robinson, P. A. 1989, ApJL, 341, L99, doi: 10.1086/185467

Roelof, E. C. 1969, in Lectures in High-Energy Astrophysics, ed. H. Ögelman & J. R. Wayland, 111

Scherrer, P. H., Schou, J., Bush, R. I., et al. 2012, SoPh, 275, 207, doi: 10.1007/s11207-011-9834-2

Schou, J., Scherrer, P. H., Bush, R. I., et al. 2012, SoPh, 275, 229, doi: 10.1007/s11207-011-9842-2

Sharma, R., Battaglia, M., Yu, S., et al. 2024, ApJ, 970, 17, doi: 10.3847/1538-4357/ad4884

Skilling, J. 1971, ApJ, 170, 265, doi: 10.1086/151210

Slottje, C. 1982

Strauss, R. D. T., & Effenberger, F. 2017, SSRv, 212, 151, doi: 10.1007/s11214-017-0351-y

Twiss, R. Q. 1958, Australian Journal of Physics, 11, 564, doi: 10.1071/PH580564

Wheatland, M. S., Sturrock, P. A., & Roumeliotis, G. 2000, ApJ, 540, 1150, doi: 10.1086/309355

Wiegelmann, T., Inhester, B., & Sakurai, T. 2006, SoPh, 233, 215, doi: 10.1007/s11207-006-2092-z

Wu, C. S., & Lee, L. C. 1979, ApJ, 230, 621, doi: 10.1086/157120

Young, C. W., Spencer, C. L., Moreton, G. E., & Roberts, J. A. 1961, ApJ, 133, 243, doi: 10.1086/147019

Yousefzadeh, M., Ning, H., & Chen, Y. 2021, ApJ, 909, 3, doi: 10.3847/1538-4357/abd8d5

Yu, S., Chen, B., Sharma, R., et al. 2024, Nature Astronomy, 8, 50, doi: 10.1038/s41550-023-02122-6

Zaitsev, V. V., & Stepanov, A. V. 1975, A&A, 45, 135

Zhang, M. 1999, ApJ, 513, 409, doi: 10.1086/306857

Zhang, Z., Chen, Y., Ni, S., et al. 2022, ApJ, 939, 63, doi: 10.3847/1538-4357/ac94c6

Zhong, Z., Guo, Y., Ding, M. D., Fang, C., & Hao, Q. 2019, ApJ, 871, 105, doi: 10.3847/1538-4357/aaf863

Zlobec, P., Messerotti, M., Li, H. W., Barry, M. B., & Comari, M. 1987, SoPh, 114, 375, doi: 10.1007/BF00167352

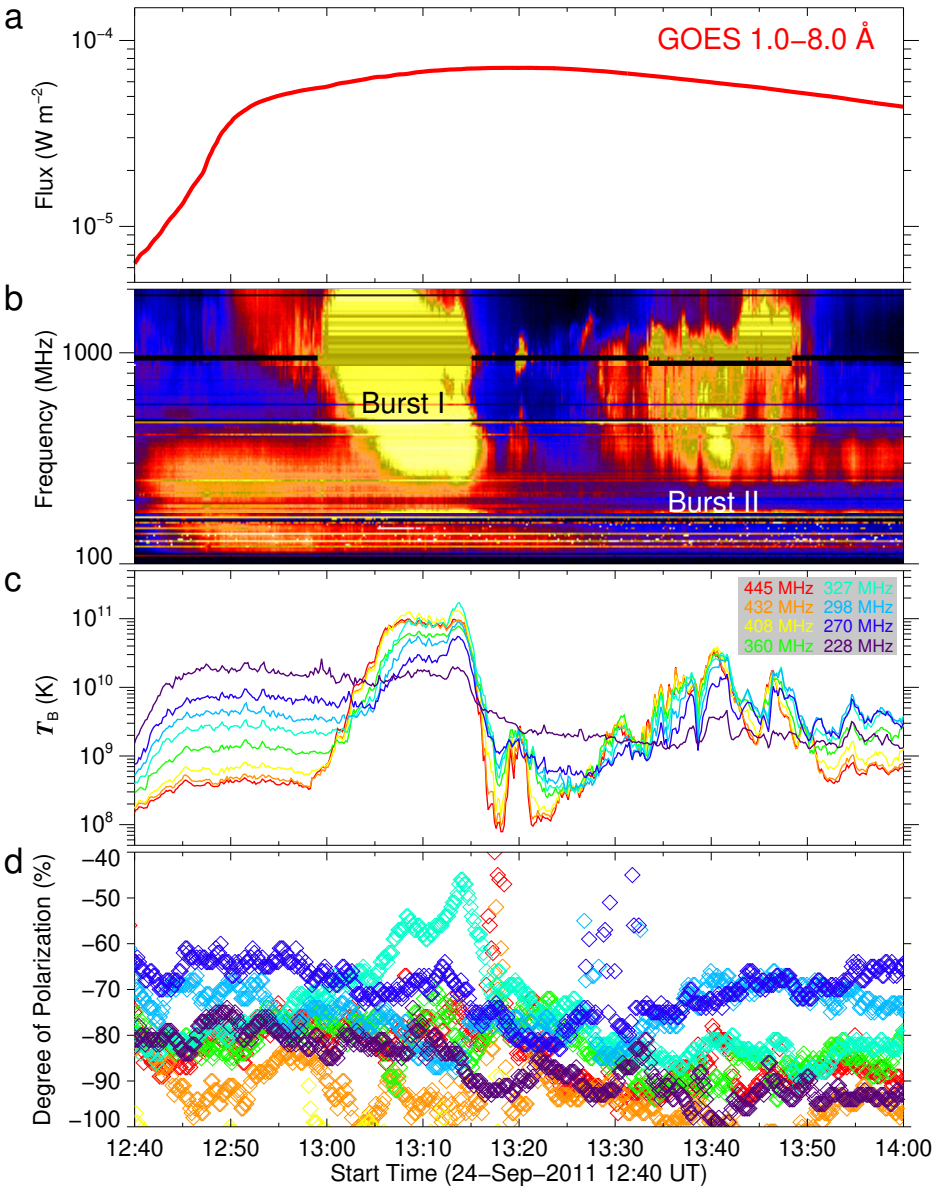

Figure 1. Overview of the t-IVdm radio burst observed on 24 September 2011. (a) GOES soft X-ray fluxes of the M7.1-class flare at 1.0–8.0 Å. **(b)** The dynamic spectra observed from 12:40 to 14:00 UT, combining the data from the San Vito observatory (100–175 MHz), the Bleien observatory (175–870 MHz), and the Ondrejov observatory (870–2000 MHz). Bursts I and II are two components of the t-IVdm event. **(c)** The temporal profiles of the maximum T_B and the degree of polarization **(d)** with a 10s cadence at 8 NRH frequencies from 228 to 445 MHz. The polarization level is obtained by taking average over the 85% contours of the maximum T_B.

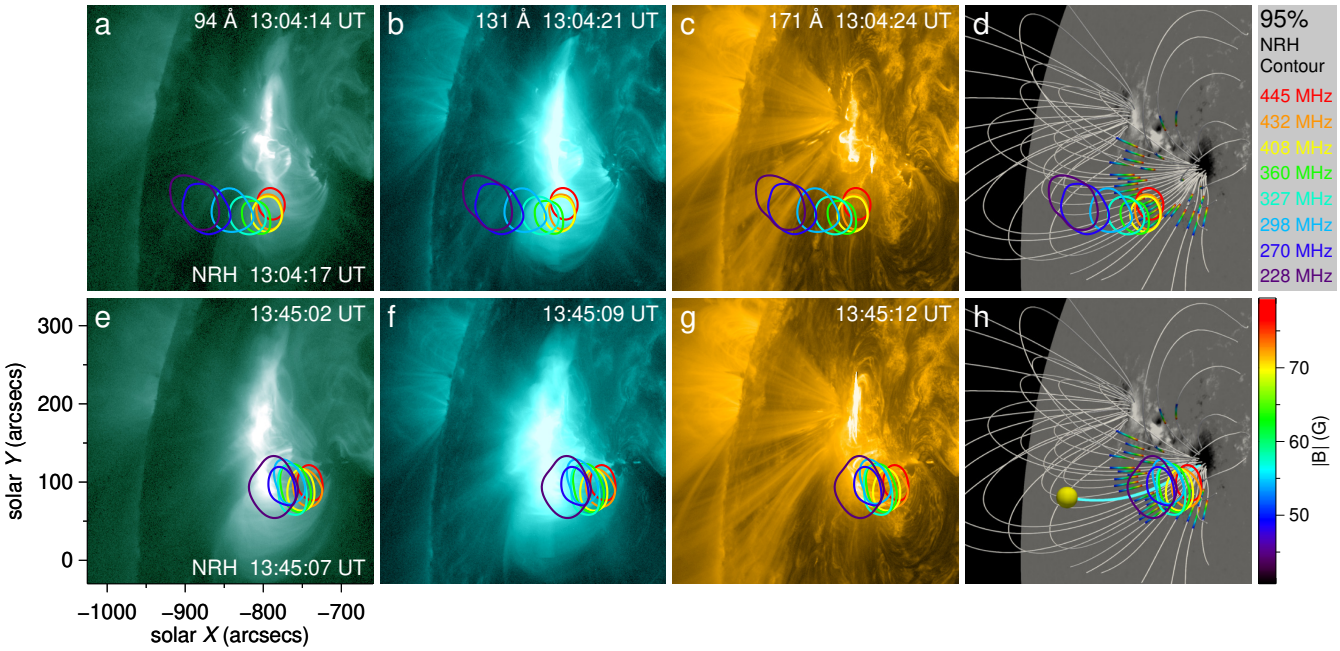

Figure 2. The AIA and HMI data of the event. (a–c) and **(e–g)** The AIA images at 94, 131, and 171 Å are overlaid with NRH 95% contours of the maximum T_B observed at 8 frequencies (228–445 MHz) for representitive moments of bursts I and II. **(d)** and **(h)** The HMI magnetogram superposed by extrapolated NLFFF field lines. The colored sections of field lines correspond to the field strengths increasing from ∼40.7 to ∼79.5 G and the corresponding 2 Ω_{ce} increasing from 228 to 445 MHz. Colored circles display NRH 95% contours at 13:04:17 **(d)** and 13:45:07 UT **(h)**. The yellow sphere crossing the cyan field line marks the location where energetic electrons are injected for the particle-transport simulation. An animation of this figure is available. It presents the temporal evolution of the radio sources and EUV structures from 12:40 UT to 14:00 UT.

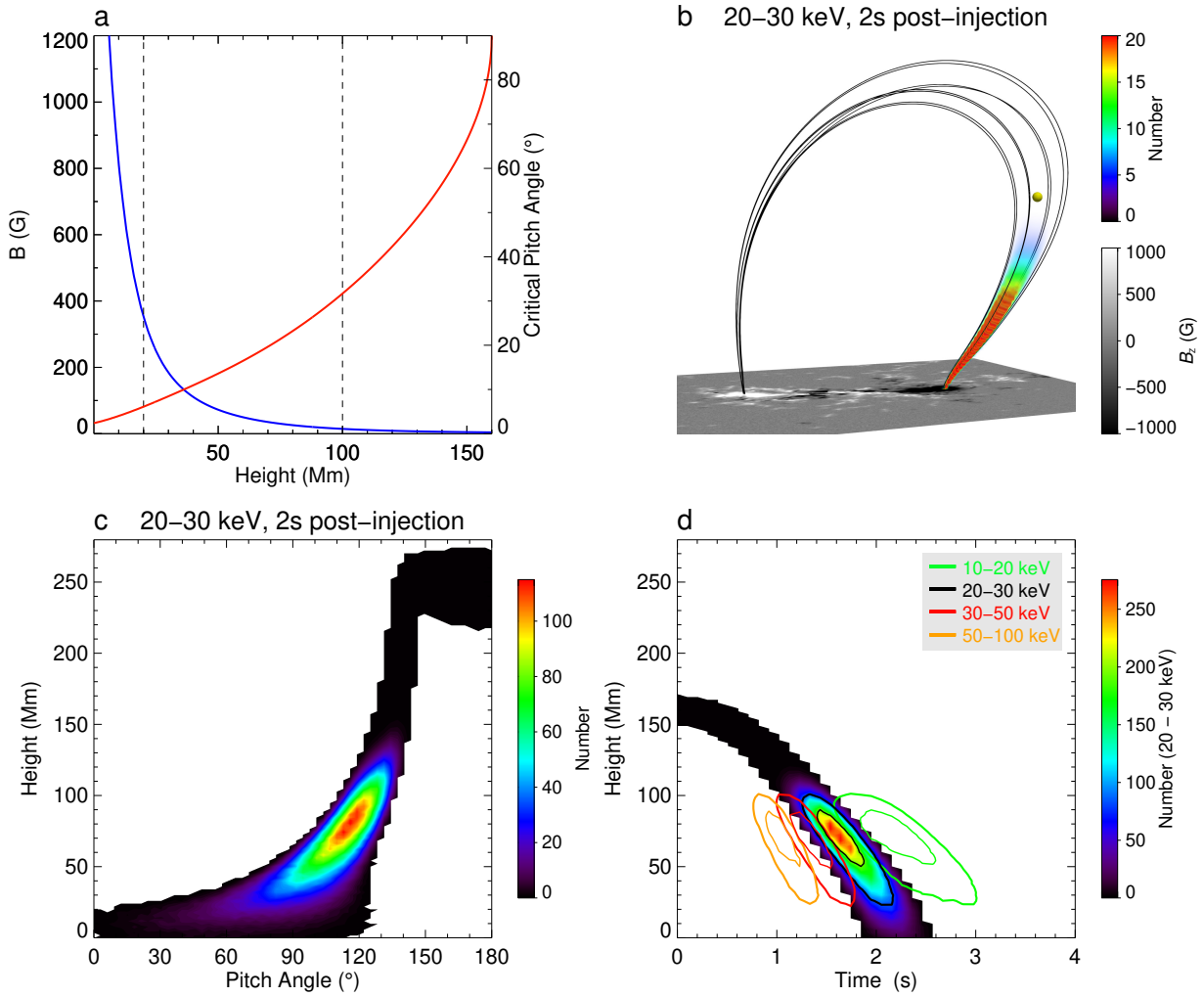

Figure 3. Modeling results of the particle transport along the selected magnetic loop. **(a)** Blue and red lines show the profiles of the magnetic field strength and critical pitch angles θ_c along the selected cyan field line plotted in Fig. 2**(h)**. The two vertical dashed lines delineate altitude range of 20 to 100 Mm. **(b)** The 3D spatial distribution at different altitudes (along the z-direction) of 20–30 keV electrons, 2s post-injection. The bottom map represents the HMI magnetogram. The yellow sphere marks the injection spot (see Fig. 2**(h)**). **(c)** The pitch angle distribution of 20–30 keV electrons versus the alitutude (z) above the solar surface. **(d)** The altitudes of mirroring points (where the pitch angle $\theta = 90^\circ$) of 20–30 keV electrons as a function of time, overplotted with the 30% and 70% contours of the respective maxima, contours at different energy bands are also plotted. Approximately 89.7% of electrons are reflected between 20 to 100 Mm for all energy ranges. An animation of panel **(b)** is available. It presents the dynamic evolution of the spatial distribution of energetic electrons along the loop.

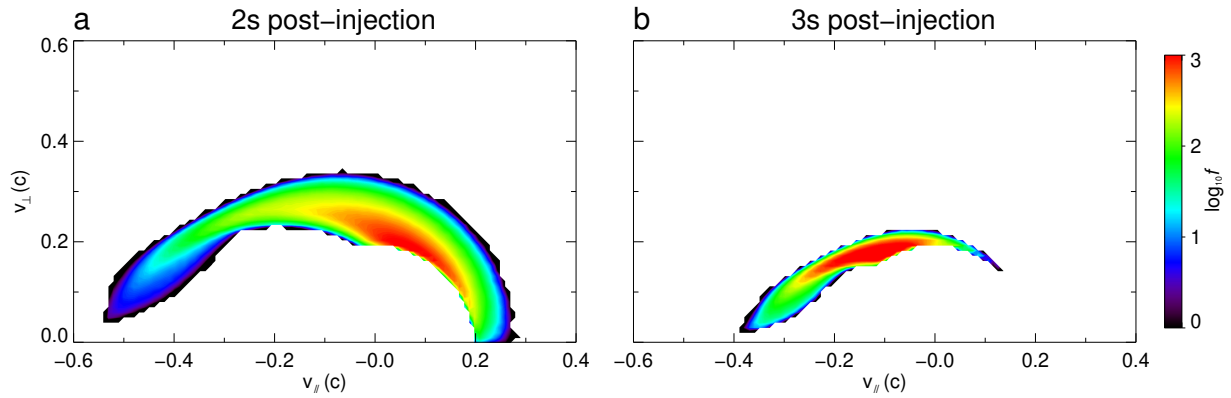

Figure 4. Velocity distribution of energetic electrons at altitudes between 20 and 100 Mm at 2s (a) and 3s (b) post-injection, respectively.

Table 1. Main information of the t-IVdm bursts and the 37 flare-associated events

No. Date	Time (UT)	Sunspot Polarity	Active Region	Flare Class	Location of Sunspot[1] (arcsecond)	Location of NRH Source at 445 MHz[2] (arcsecond)	Frequency Range (GHz)	T_B Max. (K)	Polarization Max.[3] (%)
01. 20100814	09:40-10:50	Leading (Positive) Following (Negative)	11099	C4.4	(780, 200)	(800, 50)	∼0.1–3.0	4.4×10^9 (150 MHz)	72 (360 MHz)
02. 20110307	14:16-14:45	Leading (Negative)	11166	M1.7	(-300, 250)	(-150, 350)	∼0.1–>2.0	1.2×10^{10} (150 MHz)	70 (360 MHz) -100 (445 MHz)
03. 20110809	08:31-08:56	Leading (Negative) Following (Positive)	11263	X6.9	(850, 250)	(910, 80)	∼0.2–0.6	2.2×10^9 (270 MHz)	66 (150 MHz)
04. 20110924	12:50-13:50	Leading (Negative)	11302	M7.1	(-730, 120)	(-730, 100)	∼0.2–>2.0	2.0×10^{11} (327 MHz)	-95 (432 MHz)
05. 20110925	09:40-10:40	Single (Positive)	11299	M1.5	(780, -500)	(950, -490)	∼0.2–1.2	3.8×10^8 (327 MHz)	69 (445 MHz)
06. 20111005	11:14-11:24	Leading (Positive) Following (Negative)	11313	C6.1	(-900, -250)	(-980, -360)	∼0.2–1.2	2.5×10^8 (432 MHz)	-65 (408 MHz)
07. 20120304	10:35-12:15	Leading (Positive) Following (Negative)	11429	M2.0	(-820, 330)	(-70, 420)	∼0.2–>2.0	1.0×10^{10} (360 MHz)	91 (445 MHz)
08. 20120314	15:17-15:26	Single (Positive)	11432	M2.8	(-300, -250)	(-60, 320)	∼0.2–>2.0	1.0×10^9 (228 MHz)	-32 (432 MHz)
09. 20120418	12:51-13:40	Single (Positive)	11462	C8.9	(450, -350)	(590, -340)	∼0.1–0.6	2.5×10^9 (150 MHz)	100 (408 MHz)
10. 20120427	08:22-08:27	Leading (Negative)	11466	M1.0	(500, 250)	(600, 250)	∼0.3–1.2	2.3×10^8 (445 MHz)	-10 (445 MHz)
11. 20120507-1	14:07-14:20	Single (Positive)	11471	M1.9	(630, -320)	(820, -220)	∼0.1–1.0	3.1×10^8 (150 MHz)	10 (270 MHz)
12. 20120507-2	14:36-14:41	Single (Positive)	11471	M1.9	(630, -320)	(780, -250)	∼0.2–0.5	2.2×10^8 (228 MHz)	32 (228 MHz)

Table 1 *continued*

Table 1 *(continued)*

No. Date	Time (UT)	Sunspot Polarity	Active Region	Flare Class	Location of Sunspot[1] (arcsecond)	Location of NRH Source at 445 MHz[2] (arcsecond)	Frequency Range (GHz)	T_B Max. (K)	Polarization Max.[3] (%)
13. 20120613	13:00-13:50	Leading (Positive) Following (Negative)	11504	M1.2	(-240, -300) (-390, -250)	(-150, -450) (-400, -450)	∼0.1–0.5	3.0×10^9 (150 MHz)	90 (445 MHz) -90 (408 MHz)
14. 20120614	13:40-15:15	Following (Negative)	11504	M1.5 M1.9	(-190, -250)	(-170, -300)	∼0.1–0.5	2.0×10^{10} (150 MHz)	-95 (408 MHz)
15. 20120630	08:26-08:44	No sunspot	11514	C4.4		(-400, -210)	∼0.2–0.5	6.8×10^8 (270 MHz)	-22 (432 MHz)
16. 20120708	10:23-10:30	Leading (Positive) Following (Negative)	11515	M1.1 C6.9 C5.4	(850, -300)	(930, -340)	∼0.2–0.5	8.9×10^7 (228 MHz)	-29 (228 MHz)
17. 20120710	08:37-08:45	Leading (Positive)	11519	C4.5	(-300, -300)	(-220, -310)	∼0.3–0.7	1.7×10^8 (445 MHz)	16 (327 MHz)
18. 20120816	12:56-13:06	Single (Negative)	11543	C5.2	(570, 300)	(550, 300)	∼0.1–>0.9	1.5×10^8 (327 MHz)	80 (408 MHz)
19. 20130403	09:38-09:45	Leading (Negative)	11708	C2.7	(80, 300)	(100, 300)	∼0.1–0.8	9.0×10^9 (150 MHz)	-90 (298 MHz)
20. 20130517	08:50-09:08	Following (Negative) Leading (Positive)	11748	M3.2	(-550, 190) (-450, 250)	(-620, 250) (-470, 420)	∼0.2–1.0	3.0×10^9 (408 MHz)	-50 (408 MHz) 80 (445 MHz)
21. 20130522	13:10-13:17	Single (Negative)	11745	M5.0	(900, 220)	(910, 280)	∼0.2–0.6	8.1×10^7 (298 MHz)	76 (445 MHz)
22. 20130605	08:41-09:03	Leading (Positive)	11762	B7.0 M1.3	(700, -450)	(920, -460)	∼0.2–0.5	1.4×10^9 (270 MHz)	-73 (445 MHz)
23. 20130812	10:40-11:36	Multi-sunspots	11817	M1.5	(-250, -450)	(-260,-370)	∼0.1–2.0	5.9×10^8 (150 MHz)	79 (445 MHz)
24. 20131025	14:59-15:10	Leading (Positive) Following (Negative)	11882	C7.9 X2.1	(-850, -200)	(-890, -290)	∼0.2–>0.9	1.3×10^9 (445 MHz)	46 (327 MHz)
25. 20131026-1	11:01-11:07	Leading (Positive) Following (Negative)	11882	M1.8	(-780, -200)	(-850, -100)	∼0.2–0.8	6.4×10^8 (270 MHz)	67 (445 MHz)

Table 1 *continued*

Table 1 *(continued)*

No.	Date	Time (UT)	Sunspot Polarity	Active Region	Flare Class	Location of Sunspot[1] (arcsecond)	Location of NRH Source at 445 MHz[2] (arcsecond)	Frequency Range (GHz)	T_B Max. (K)	Polarization Max.[3] (%)
26.	20131026-2	11:15-11:41	Leading (Positive) Following (Negative)	11882	M1.8	(-780, -200)	(-820, -220)	∼0.2–1.4	4.7×10^9 (445 MHz)	94 (445 MHz)
27.	20131107-1	12:24-12:29	Following (Negative)	11890	C5.9	(-350, -300)	(-320, -500)	∼0.3–2.6	1.0×10^8 (408 MHz)	-15 (408 MHz)
28.	20131107-2	14:30-15:10	Following (Negative)	11890	M2.4	(-350, -300)	(-340, -660)	∼0.3–0.5	1.9×10^8 (327 MHz)	-100 (408 MHz)
29.	20131119	10:20-10:25	Multi-sunspots	11893	X1.0	(870, -220)	(960, -360)	∼0.4–>2.0	1.9×10^8 (445 MHz)	-20 (408 MHz)
30.	20140216-1	09:23-09:35	Multi-sunspots (Positive)	11977	M1.1	(-50, -50)	(50, -150)	∼0.2–0.6	2.5×10^{10} (408 MHz)	100 (228, 408, 432 MHz)
31.	20140216-2	13:50-14:05	Single (Positive)	11977	C3.4	(0, -50)	(100, -100)	∼0.2–>0.9	5.0×10^9 (228 MHz)	95 (228 MHz)
32.	20140319	12:50-12:55	Multi-sunspots	12012	C1.6 C3.3	(900, -220)	(-1150, -50)	∼0.2–0.6	3.0×10^9 (228 MHz)	15 (270 MHz)
33.	20140404	13:36-13:45	Single (Negative)	12027	C8.3	(-370, 300)	(-400, 550)	∼0.1–>2.0	7.0×10^9 (150 MHz)	10 (270 MHz)
34.	20140415	09:16-09:26	Single (Positive)	12035	C8.6	(-420, -180)	(-400, -150)	∼0.2–>0.9	1.0×10^8 (327 MHz)	70 (445 MHz)
35.	20140728	14:01-14:06	Leading (Positive)	12125	C2.4	(-700, -260)	(-750, -200)	∼0.4–>0.8	1.5×10^7 (445 MHz)	95 (432 MHz)
36.	20140821	11:57-12:05	Following (Positive)	12148	C1.2	(-570, 0)	(-620, -50)	∼0.2–0.6	3.0×10^8 (298 MHz)	95 (408 MHz)
37.	20140918	08:39-08:45	Single (Negative)	12169	M1.2	(-850, 120)	(-1000, 120)	∼0.1–0.8	3.0×10^{11} (150 MHz)	60 (327 MHz) -40 (432 MHz)

[1]When more than one sunspot is observed, the location of the sunspot that is closest to the radio sources is presented. When the sunspots are close to each other (e.g. they are near the limb), an average location is presented.

[2]The coordinates represent the average location during the event.

[3]When the sense of polarization shows a significant inversion during the event, the values for both senses are presented.

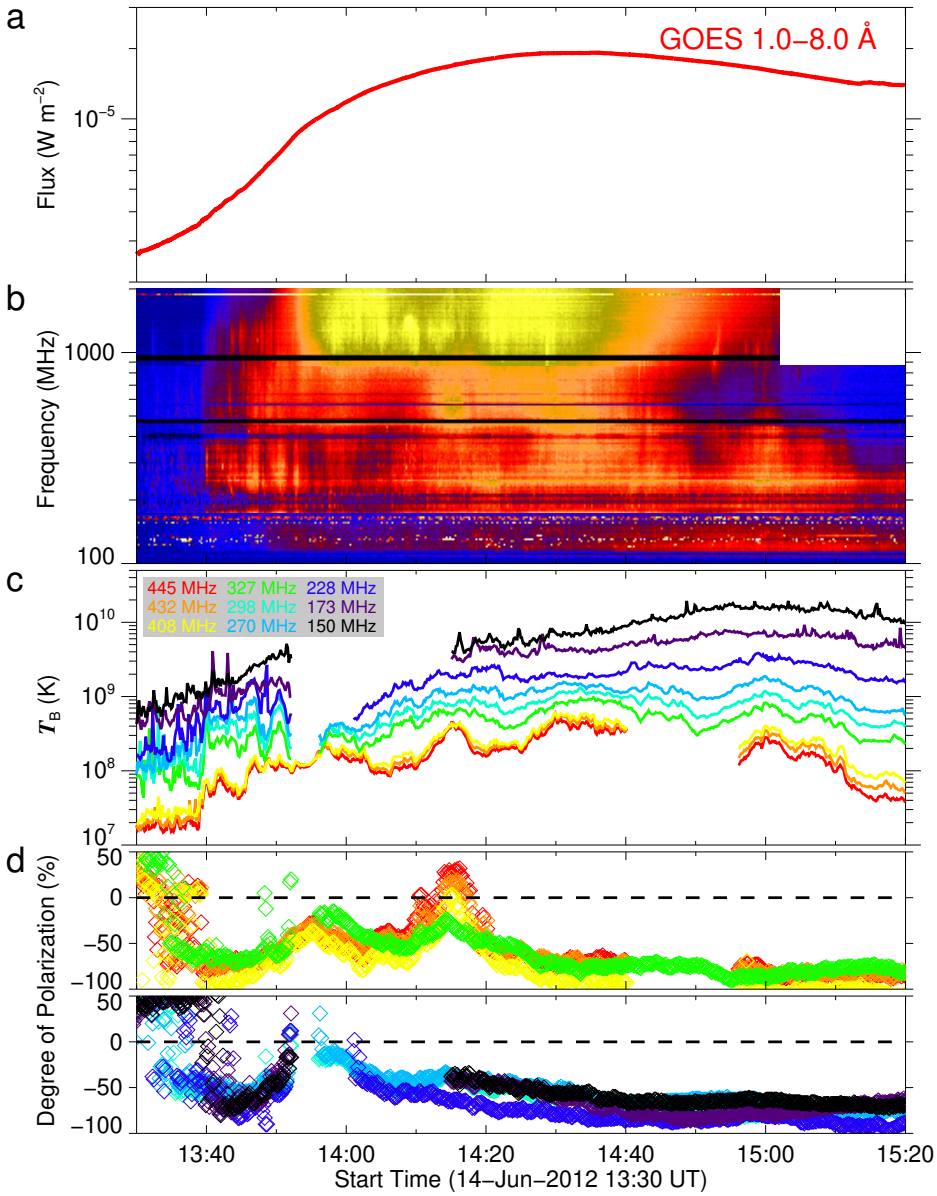

Figure S1. Overview of the radio burst observed on 14 June 2012. (a) GOES soft X-ray fluxes of the M1.9-class flare at 1.0–8.0 Å. **(b)** The dynamic spectra observed from 13:30 to 15:20 UT, combining the data from the San Vito observatory (100–175 MHz), the Bleien observatory (175–870 MHz), and the Ondrejov observatory (870–2000 MHz). **(c)** Temporal profiles of the maximum T_B and **(d)** the degree of polarization with 10s cadence at 9 NRH frequencies from 150 to 445 MHz. The polarization level is obtained by averaging data over the 85% contours of the maximum T_B. Data gaps correspond to sources far away from the sunspots.

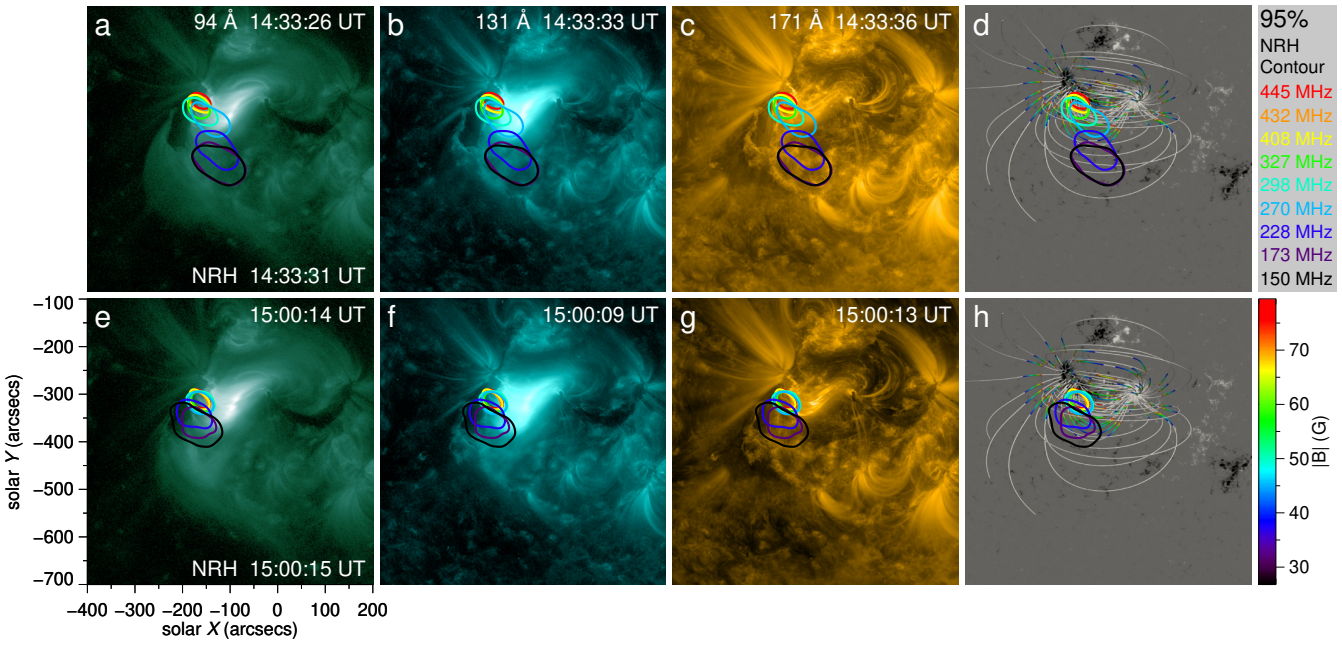

Figure S2. The AIA and HMI data of the 20120614 event. (a–c) and **(e–g)** The AIA images at 94, 131, and 171 Å are overlaid with the NRH 95% contours of the maximum T_B at 9 frequencies (150–445 MHz) for two representative moments. **(d)** and **(h)** The HMI magnetogram superposed by extrapolated NLFFF field lines. The colored sections of field lines correspond to the field strengths increasing from ∼26.8 to ∼79.5 G and the corresponding 2 Ω_{ce} increasing from 150 to 445 MHz. Colored circles display NRH 95% contours at 14:33:31 and 15:00:15 UT respectively. An animation of this figure is available. It presents the temporal evolution of the radio sources and EUV structures from 13:30 UT to 15:20 UT.